buildings

MDPI

Article

Study on the Dynamic Performance and Damage Evaluation of Rubber-Modified Non-Autoclaved Concrete Pipe Piles under Axial Drop Hammer Impact

Sheng Lan [1], Feng Liu [1], Fei Yang [1,*], Wanhui Feng [2] and Dawei Chen [1]

[1] School of Civil and Transportation Engineering, Guangdong University of Technology, Guangzhou 510006, China; 1112009004@mail2.gdut.edu.cn (S.L.); fliu@gdut.edu.cn (F.L.); 2112009178@mail2.gdut.edu.cn (D.C.)
[2] College of Urban and Rural Construction, Zhongkai University of Agriculture and Engineering, Guangzhou 510225, China; whfeng@zhku.edu.cn
* Correspondence: feiyang730@gdut.edu.cn

Abstract: In order to improve the weak impact resistance of non-autoclaved concrete pipe piles, this study replaced sand in the concrete with rubber particles of different volume contents to obtain rubber-modified non-autoclaved concrete pipe piles (with volume contents of 0%, 5%, 10%, and 15%). The dynamic impact response characteristics of rubber-modified non-autoclaved concrete pipe piles were obtained through large-scale axial hammer impact experiments. The results indicate the following. (1) Non-autoclaved concrete pipe piles without rubber additives were prone to expansion deformation instability under impact. When the rubber content was 10%, the expansion deformation of the piles was the weakest, and the state was the most stable. (2) When the impact energy exceeded 48 kJ, the deformation energies of piles with 5% and 10% rubber contents significantly increased. (3) The damage levels of the piles after hammer impact were classified into four grades: no damage, mild damage, moderate damage, and severe damage. When the impact energy was greater than or equal to 48 kJ, rubber-modified non-autoclaved concrete pipe piles exhibited damage. The zone with no damage for piles with 10% rubber content was the smallest, making it less prone to damage under impact loads. The rubber-modified non-autoclaved concrete pipe piles with 10% rubber content not only had excellent impact resistance but also utilized the advantages of being environmentally friendly and energy-saving. They filled a certain knowledge gap in green building materials.

Keywords: rubber-modified non-autoclaved concrete pipe piles; drop hammer impact; impact energy; damage level; three-dimensional digital speckle technology

check for updates

Citation: Lan, S.; Liu, F.; Yang, F.; Feng, W.; Chen, D. Study on the Dynamic Performance and Damage Evaluation of Rubber-Modified Non-Autoclaved Concrete Pipe Piles under Axial Drop Hammer Impact. *Buildings* **2024**, *14*, 489. https://doi.org/10.3390/buildings14020489

Academic Editor: Binsheng (Ben) Zhang

Received: 13 January 2024
Revised: 6 February 2024
Accepted: 7 February 2024
Published: 9 February 2024

Copyright: © 2024 by the authors. Licensee MDPI, Basel, Switzerland. This article is an open access article distributed under the terms and conditions of the Creative Commons Attribution (CC BY) license (https://creativecommons.org/licenses/by/4.0/).

1. Introduction

The current prestressed high-strength concrete pipe piles (PHC piles) mainly adopt steam curing and high-temperature and high-pressure secondary curing technology, which allows for the rapid attainment of PHC piles that meet the usage requirements within 24 h. However, the energy consumed during the production of pipe piles is mainly derived from coal [1]. Burning coal generates a large amount of harmful gases such as sulfur dioxide and nitrogen oxides, causing pollution to the environment. In 2020, the carbon emissions from China's construction industry accounted for 50.9% of the country's total carbon emissions, with building material production accounting for 28.2% [2]. In order to reduce carbon emissions and achieve the goals of the 'dual-carbon' strategy, all pipe pile factories were required to cease the use of coal and instead utilize natural gas, which has lower pollution levels. However, not only did natural gas incur higher costs, but its carbon emissions were also not low. The emission of CO and CO_2 after the combustion of natural gas per cubic meter can reach 21.2 kg and 6.7 kg, respectively [3]. In this context, the non-autoclaved curing technology has emerged. This technology

eliminates the need for the second round of high-temperature and high-pressure curing in traditional methods and only involves steam curing. As the non-autoclaved curing technology eliminates the high-temperature and high-pressure curing steps, the production cost is significantly reduced. According to Chinese standards, the carbon emissions from the non-autoclaved curing process were reduced by 17.2% compared to autoclaved curing pipe piles (AP) [4]. In addition, compared to AP concrete, non-autoclaved pipe piles (NAP) concrete exhibited significant improvements in frost resistance, sulfate resistance, strength, and other properties [5–7].

The compressive strength of NAP concrete could reach 90 MPa [8]. However, similar to many high-strength concretes, NAP concrete also exhibited a high brittleness index with a tensile–compressive strength ratio of only 0.043 [9]. And its dynamic compression enhancement factor was mostly within the range of 1.0~1.2, which was smaller than that of AP concrete [9]. Liu et al. [10] conducted drop hammer impact tests on NAP and AP, and found that under high-energy impact, NAP experienced failure first. In practical applications, under impact loads such as hammering piles and earthquakes, NAP was prone to brittle failure. Water from the external environment could enter the pile body through cracks and corrode the steel bars, greatly affecting the performance of the pipe piles. This defect has seriously affected the widespread application of non-autoclaved curing technology. In addition, high temperatures during a fire caused significant damage to the strength of ordinary concrete [11]. To improve the mechanical performance of concrete, researchers often add glass fibers and expansion agents to concrete and even used steel structures [12–14]. However, these methods have shown limited effectiveness in enhancing the impact resistance of concrete. On the other hand, with the rapid development of China's automotive industry, the pressure caused by waste tires on the environment is increasing. In 2022 alone, the number of scrap tires in China reached approximately 350 million, and this number is still growing at an annual rate of 6% to 8% [15]. Some experts and scholars uphold the concept of green energy-saving and have attempted to crush the rubber materials in waste tires into particles and add them to the concrete. This approach had yielded recycled rubber concrete with lower brittleness and higher impact resistance [16–21]. Our team attempted to incorporate recycled rubber particles into NAP concrete to produce rubber-modified non-autoclaved pipe pile (NAPR) concrete. It was found that the addition of recycled rubber significantly enhanced the crack resistance and impact resistance of NAPR concrete [9].

Although there have been some achievements in the research on NAPR concrete materials, the research at the component level is still lacking, especially regarding its impact resistance performance, which remains unclear. In practical engineering, pipe piles are prone to impact damage during hammering pile construction. Based on this background, this study investigates the dynamic impact response characteristics of NAPR through axial falling hammer impact experiments and explores the influence of recycled rubber on the impact resistance performance of NAPR.

2. Preparation of Non-Autoclaved Concrete Pipe Piles

2.1. Concrete Materials for Non-Autoclaved Pipe Piles

Due to the omission of energy-intensive high-temperature and high-pressure curing steps in NAP, the fine grinding sand in the original concrete mix cannot react to form tobermorite [22]. As a result, the strength of the concrete cannot meet the strength requirements specified in relevant Chinese standards for prestressed high-strength concrete pipe piles, which is greater than 80 MPa [23]. To meet this standard, slag powder and silica powder were used to replace fine grinding sand to enhance the concrete strength. The specific mix proportions are listed in Table 1.

Table 1. Mix proportions of concrete (kg/m^3).

Cement	1–2 Stones	0–5 Stones	Sand	Slag Powder	Silica Powder	Water Reducer (Solid Content 40%)	Water	Water to Glue Ratio
282	910	310	705	141	47	5.64	100	0.213

As shown in Figure 1, the cement selected was P.II 42.5R Portland cement produced by China Resources Cement Limited in Jiangmen City, Guangdong Province, China. The sand chosen was medium sand with a fineness modulus of 2.6. The specific surface areas of slag powder and silica powder were 412 m^2/kg and 21 m^2/kg, respectively. The water reducer was QL-PC5 type polycarboxylate high-efficiency water reducer with a solid content of 40% produced by Jiangmen Strong Building Materials Technology Co., Ltd. in Jiangmen City, Guangdong Province, China. In order to enhance the impact resistance of NAP, rubber particles with a diameter of 0.85 mm were used for partial replacement of sand in a volume substitution method, with replacement rates of 5%, 10%, and 15%.



(**a**) Cement (**b**) Sand (**c**) Rubber particles

(**d**) Water reducer (**e**) Slag powder (**f**) Silica powder

Figure 1. Raw materials for the concrete part of NAPR.

2.2. Forming of Non-Autoclaved Concrete Pipe Piles

2.2.1. Production Process

As shown in Figure 2, several important preparation steps of the NAPR fabrication process include concrete mixing, mixture filling, prestress application, centrifugal molding, and steam curing. NAPR needs to be cured in a 90 °C steam chamber for twenty-four hours, after which the cover can be removed and the mold dismantled.



Figure 2. Preparation process of NAPR.

Figure 3 depicts the finished product of NAPR. From the figure, it can be observed that compared to AP, NAPR has an overall darker color, appearing as deep gray. The surface of the pile body is smooth and free from defects. The pipe piles are in a standard cylindrical shape without any deformation. The inner wall of the piles is smooth, with an intact protective layer and no exposed sand or gravel. The formed NAPR meets the structural requirements of high-strength prestressed piles [24].

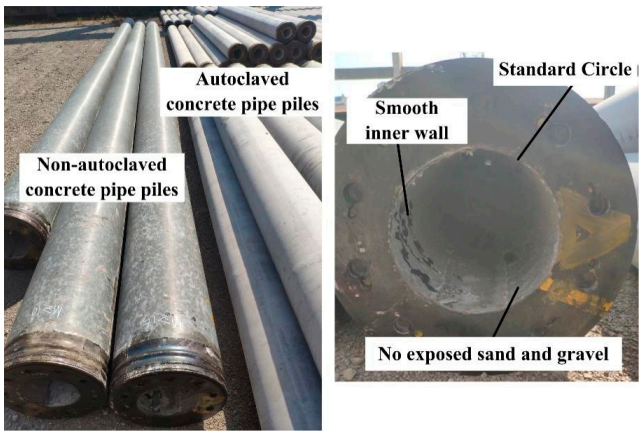


Figure 3. Appearance of NAPR.

2.2.2. Parameters of Pipe Piles

Prestressed high-strength concrete piles are divided into four major categories: A type, AB type, B type, and C type. For construction projects, A type and AB type can meet most requirements. The vertical bearing capacities of these two types of piles are the same. The non-autoclaved pipe piles prepared in this study were of the A type, and the structure and some of the reinforcing parameters of the piles are listed in Table 2. Combined with Figure 4, it can be seen that the outer diameter of the pile was 400 mm, and the wall thickness was 95 mm. Since this study focuses on the vertical impact resistance of NAPR and does not involve the bending resistance of the piles, in order to control variables, the dense area of spiral hoops was removed, and the spacing between all spiral hoops was selected as 80 mm.

Table 2. Structural parameters of NAPR (mm).

Specifications and Dimensions			Prestressed Steel Reinforcement			Stirrup
Outside Diameter	Wall Thickness	Length	Diameter	Distribution Diameter	Diameter	Distance
400	95	12,000	9	308	4	80 ± 5

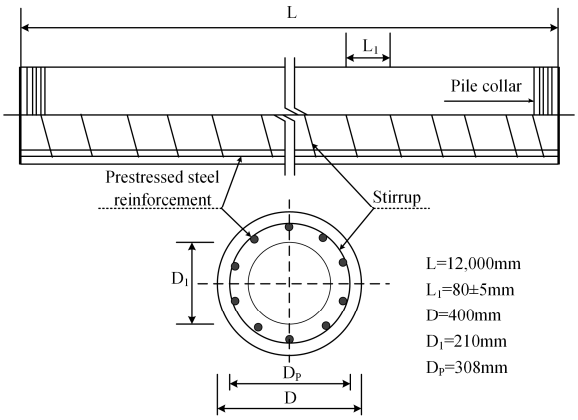


Figure 4. Schematic diagram of NAPR structure.

The study only focuses on the axial impact resistance test of NAPR, without considering the impact stability of the piles and the influence of length. As shown in Figure 5, the full-length piles were cut into one-meter-long short piles according to the experimental conditions, and the end faces of the piles were polished after cutting to ensure that the inclination unevenness of the end face was less than 0.5 mm [24]. For ease of analysis, the specimens of non-autoclaved pipe piles were named based on different rubber contents. For the name of NAPRX, "NAPR" refers to rubber-modified non-autoclaved pipe pile, and "X" indicates the rubber content in percentage. For example, NAPR5 represents the non-autoclaved pipe pile with a rubber content of 5%.



Figure 5. Specimens of NAPR.

3. Large-Scale Drop Hammer Impact Experiment

3.1. Experimental Equipment

The experimental equipment used for the axial drop hammer test on piles in this study was the Vertical Ultra-Heavy Drop Hammer Experimental Apparatus in the School of Transportation, Civil Engineering & Architecture at Foshan University of Science and Technology, China. As shown in Figure 6, the Vertical Ultra-Heavy Drop Hammer Experimental Apparatus mainly consisted of five parts: the base, support, rail, hammer head, and operating system, which could achieve numerical control and dynamic data acquisition. The maximum height of the drop hammer was 18 m, the maximum mass of the hammer head was 1200 kg, and the maximum impact energy was 170 kJ, which could meet the requirements of axial drop hammer impact tests on piles.

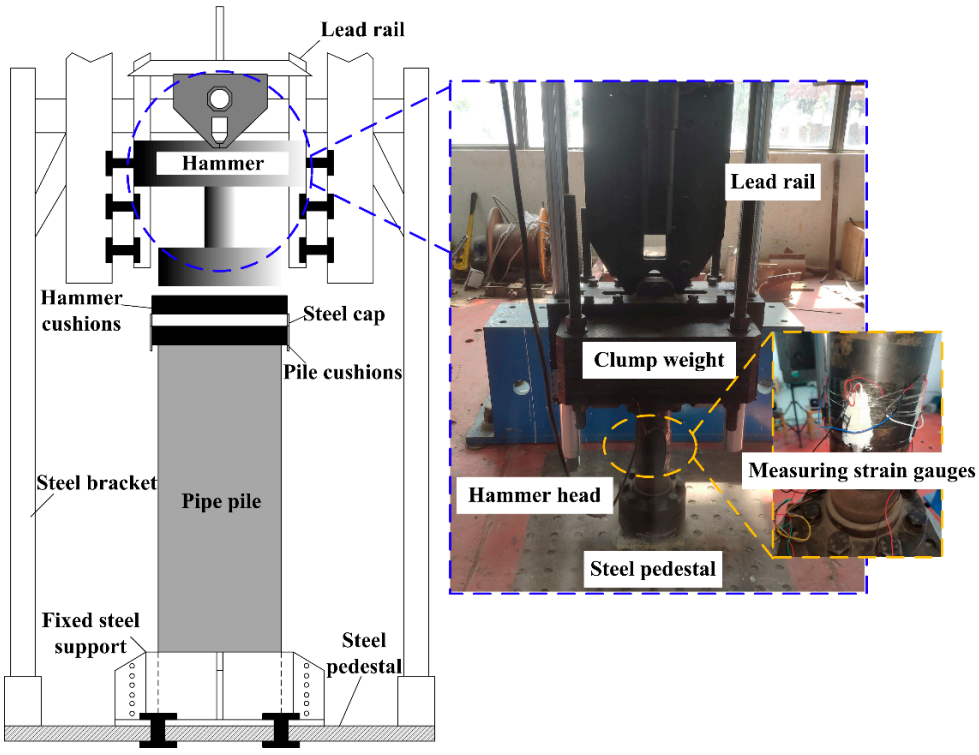


Figure 6. Vertical Ultra-Heavy Drop Hammer Experimental Apparatus.

3.2. Experimental Scheme

Before the experiment, it was necessary to fix the NAPR on the base using a custom fixture. To ensure that the impact load of the falling hammer was evenly applied to the end face of the NAPR, a steel cap with an inner diameter of 420 mm was installed at the end of the pile. In addition, to ensure the stiffness of the steel cap and reduce experimental errors caused by deformation, the thickness of the steel cap was 50 mm. In order to avoid the phenomenon of stress concentration during the drop hammer test, 30 mm thick cardboard was added as a cushion between the steel cap and the pile end. The direct impact of the hammer head on the steel cap was prone to causing damage. In order to protect the hammer head, 40 mm thick plywood was placed on the steel cap. The specific arrangement is illustrated in Figure 7. Three sets of strain gauges were pasted on the vertical surfaces of the pile body at heights of 250 mm, 500 mm, and 750 mm to obtain the axial and transverse strains of NAPR in the drop hammer test. Additionally, in order to obtain the deformation characteristics of the surface of the NAPR during the impact process of the falling hammer, a three-dimensional digital image correlation (DIC) technique was employed. Matte paint was used to spray good speckle points on the surface of the pile, and three-dimensional DIC technology could obtain the local deformation field of the pile body by calculating the displacement of the speckle points on the surface of the pile during the experimental process.

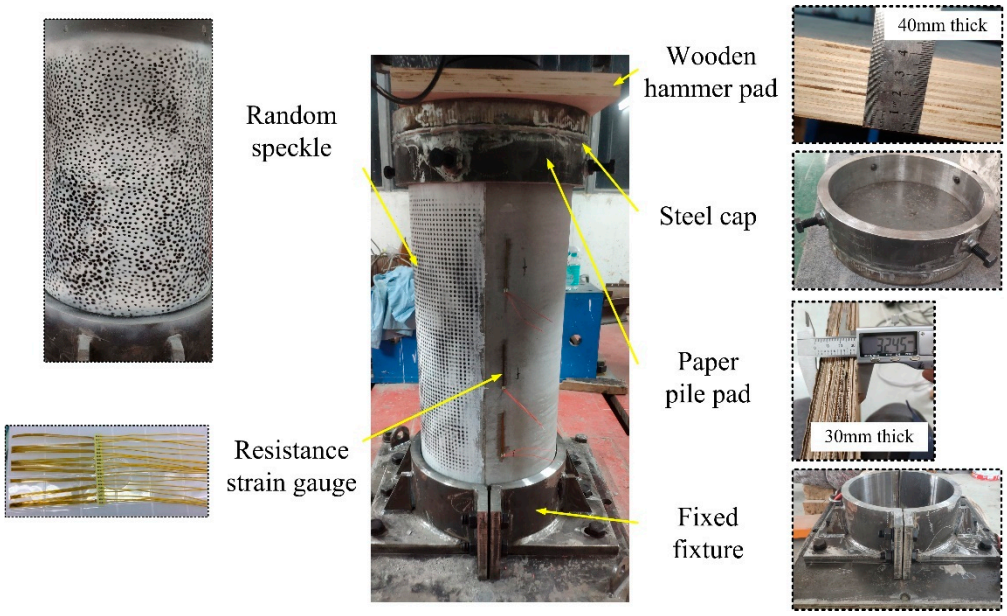


Figure 7. Preparation before the experiment.

Figure 8 is a schematic diagram of the axial drop hammer experiment for NAPR. After completing the preparation work, the high-speed cameras and drop hammer control system were calibrated and adjusted. It was found that when the two high-speed cameras were 2 m away from the piles and at an angle of 30 degrees, the calibration results were the best and the required measurement surface could be fully captured. Therefore, the two cameras were fixed at 30 degrees at a distance of 2 m from the piles [25]. Finally, the drop hammer was controlled to reach the predetermined height through the system software and complete the axial drop hammer impact experiment. During the experiment, three types of data were primarily collected: impact load, surface strains of the pile body, and high-speed speckle photos. The frequency of collecting impact load was 500 kHz, the frequency of collecting strain was 100 kHz, the resolution of the high-speed camera was 1024 × 1024, and the collection frequency was 12,500 frames per second.

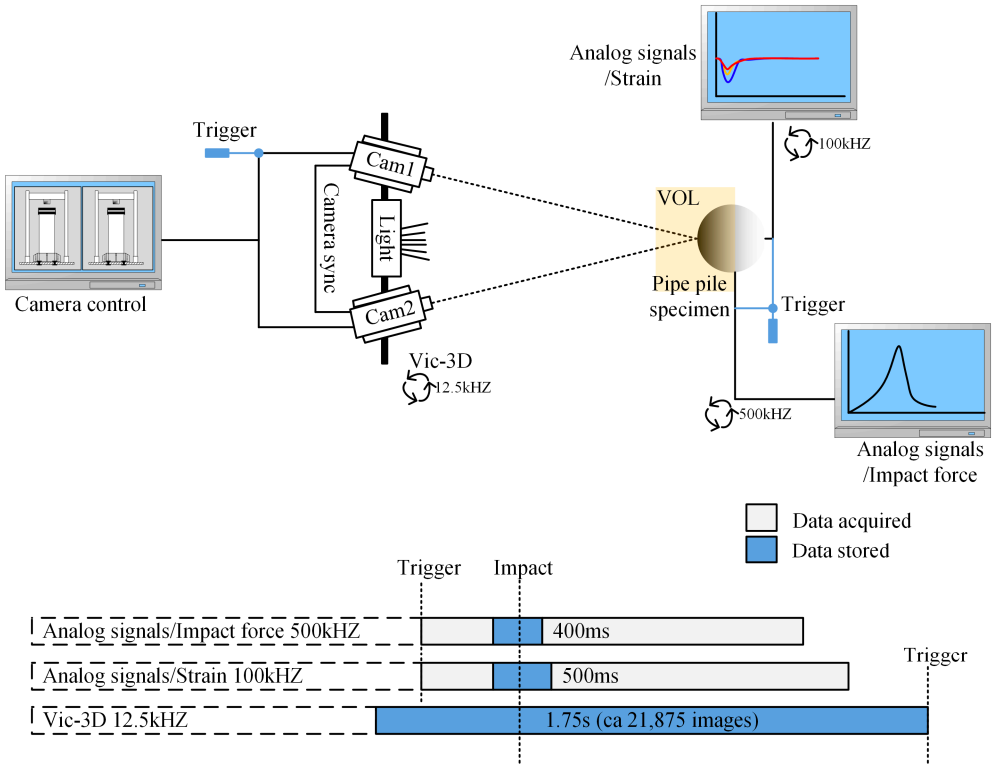


Figure 8. Schematic diagram of axial drop hammer test on NAPR.

According to Chinese standards, it is known that the maximum impact energy exerted on the piles during actual pile-driving construction will not exceed 50 kJ [26]. In this experiment, this impact energy was used as a reference to obtain the dynamic response characteristics of the piles under different impact energies by adjusting the drop hammer height. The weight of the hammer head in the drop hammer device was chosen as 1200 kg, and the experimental drop heights were 2 m, 4 m, 5 m, and 6 m, corresponding to the impact energies of 24 kJ, 48 kJ, 60 kJ, and 72 kJ, respectively.

4. Dynamic Response Characteristics of NAPR

4.1. Drop Hammer Impact Force

4.1.1. Impact Loading

The impact energies of the axial drop hammer test for NAPR with different rubber contents were controlled by the drop heights. As shown in Figure 9, the impact load on the non-steam pressure-cured piles decreased with the increase of the rubber content.

The ultimate bearing capacities of conventional precast concrete piles during pile driving ranged from 1500 kN to 3000 kN and could reach up to 4000 kN in larger cases [27–30]. However, in this experiment, the NAPR achieved a maximum dynamic bearing capacity of 5000 kN, which was significantly higher than that of conventional precast concrete piles. When the impact energy was 60 kJ, the average impact loads of NAPR with rubber contents of 0%, 5%, 10%, and 15% were 5939.7 kN, 5763.9 kN, 5702.8 kN, and 5675.7 kN, respectively. The impact loads with the addition of rubber pieces were reduced by 3%, 4%, and 4.4% compared to the impact loads without the addition of rubber pieces. When the impact energy was 72 kJ, NAPR5 exhibited the maximum impact load of 6500.4 kN.

Comparing the effect of rubber content on the impact loads of piles, it was found that when the impact energy was below 48 kJ, the impact loads were mainly influenced by the impact energy, and the effect of rubber content was relatively small. Especially when the impact energy was 24 kJ, the impact loads were not affected by the rubber content, which were the same as that of NAPR with different rubber contents. When the impact energy exceeded 48 kJ, the influence of rubber content on the impact load gradually manifested.

With the increase in rubber content, the impact loads under the same impact energy showed a trend of first increasing and then decreasing with the increase in rubber content. The impact load of NAPR was maximum when the rubber content was 5%.

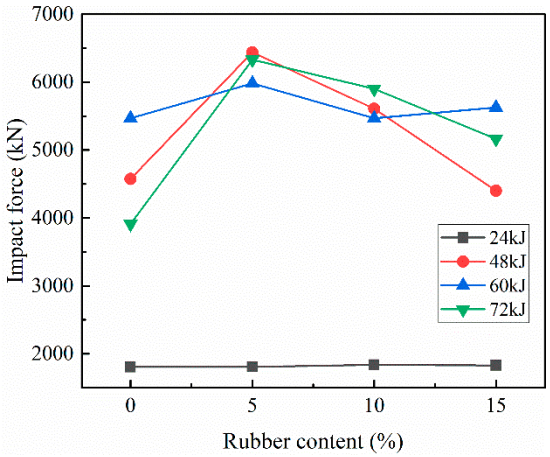


Figure 9. Relationship between impact load and rubber content for different impact energies.

4.1.2. Deformation Energy

The drop hammer impact test had a short duration, on the millisecond scale, where the drop distance of the hammer during contact with the bearing surface of the pile was used as the deformation displacement of the pile [10]. The calculation formula is shown in Equation (1).

$$z(t) = \iint \frac{F(t) - m \cdot g}{m} d^2t \quad (1)$$

where $F(t)$ is the impact load of the hammer, m is the total mass of the hammer weight, and g is the acceleration due to gravity.

In Figure 10, the impact load–displacement curves for NAPR with different rubber contents and under different impact energies are presented. The impact load increased with the increasing impact energy. At the same time, the shorter duration of the impact resulted in an increased slope of the load–displacement curve in the linear segment. Greater impact energy and shorter impact duration meant that the pile was more likely to undergo brittle failure. However, as the impact energy increased, the postpeak segment of the load–displacement curve became smoother. From the curve, it could be observed that as the rubber content increased, the difference in the peak loads decreased for each impact energy. This indicated that the trend of increasing the impact load with the increasing impact energy was diminishing. Comparing the impact loads of 60 kJ and 72 kJ, it could be observed that with the rubber contents of 5% and 10%, the impact loads increased by 19.2% and 7.9%, respectively. Interestingly, with a higher rubber content, the increase in the impact load was relatively smaller. This indicated that rubber particles have a better cushioning effect on high impact energies.

As shown in Figure 11, the deformation energy generated during the impact process of the NAPR can be regarded as a significant indicator to measure the self-energy absorption capacity of the pile. It could be observed from the figure that when the impact energy was less than 48 kJ, the deformation energies of the steam-free piles with different rubber contents were almost the same. When the impact energy exceeded 48 kJ, the deformation energy of the NAPR increased the fastest. When the impact energy exceeded 60 kJ, the deformation energies were significant for the rubber contents of 5% and 10%, measuring 25.2 kJ and 21.9 kJ, respectively. In addition, as the impact energy increased, the proportion of the deformation energy to the impact energy increased. When the impact energies were 24 kJ, 48 kJ, and 60 kJ, the deformation energies of the piles were 3.47 kJ, 10.5 kJ, and 19.3 kJ, respectively. The proportions of the deformation energy to the impact energy were 14.46%, 21.9%, and 32.2%, respectively. The reason for this was that as the impact energy increased,

especially when the impact energy exceeded 48 kJ, the pile underwent damage, resulting in significant increases in deformation. The evolution trend lines of the deformation energies of NAPR with four different rubber contents were compared. It could be observed that as the impact energy increased, the growth trends of the deformation energies of NAPR with 0% and 15% rubber contents were slowing down, while the growth trends of the deformation energies of NAPR with 5% and 10% rubber contents remained significant.

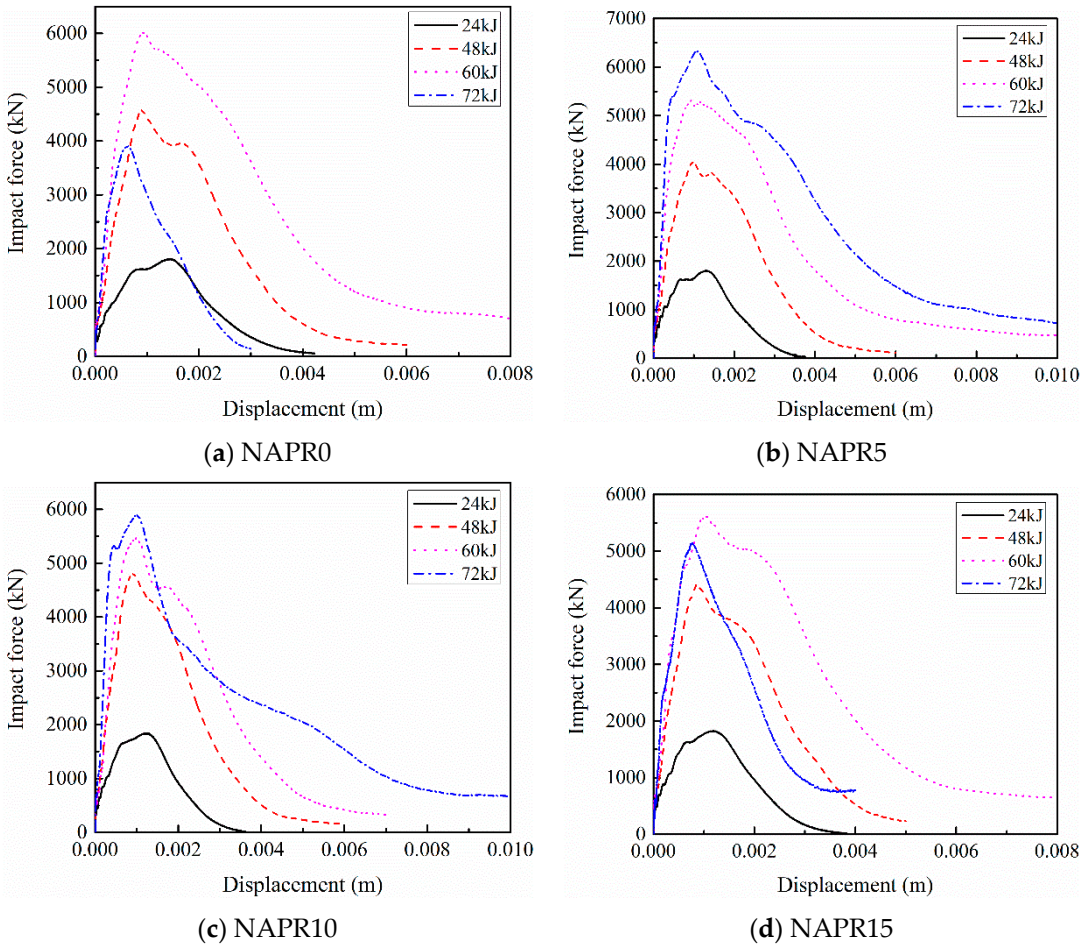


Figure 10. Impact load–displacement curves.

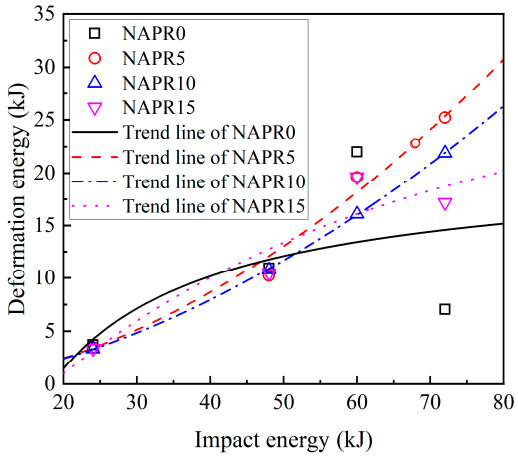
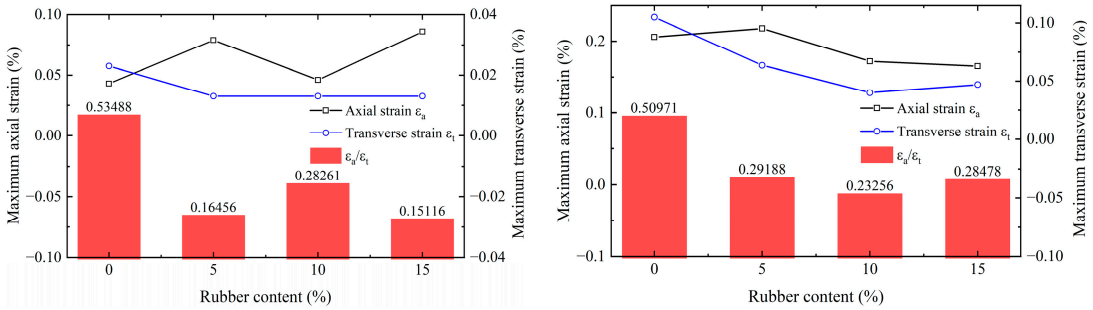


Figure 11. Relationships between the deformation energy and impact energy of NAPR with different rubber contents.

4.1.3. Strain of Pile Body

During the axial hammer impact experiment, strain gauges with a gauge length of 100 mm and a resistance of 120 Ω were attached to the pile shaft to measure the strains of the pile. As shown in Figure 12, taking the impact energies of 24 kJ and 72 kJ as examples, the axial strains, transverse strains, and lateral deformation coefficients of NAPR with different rubber contents were analyzed. Whether the impact energy was low impact energy of 24 kJ or high impact energy of 72 kJ, the axial and transverse strains of the pile both exhibited decreasing trends as the rubber content increased.



(**a**) 24 kJ (**b**) 72 kJ

Figure 12. Strain characteristics of the pipe pile body under different impact energies.

The ratio of the transverse strain to the axial strain is called the lateral deformation coefficient, which reflects the expansion deformation of the NAPR. The lateral deformation coefficient of the pile body reflects the pile's stability under impact to some extent [31,32]. From the figure, it can be seen that whether there is low impact energy (24 kJ) or high impact energy (72 kJ), the lateral deformation coefficient of the NAPR without rubber is the largest, exceeding 0.5, indicating that the NAPR without rubber is prone to expansion deformation. When the impact energy was 24 kJ, the lateral deformation coefficients of the piles with the rubber contents of 5% and 15% were relatively small, with the values of 0.16456 and 0.15116, respectively. However, when the impact energy was 72 kJ, the lateral deformation coefficients of the piles with these two rubber contents increased to 0.29188 and 0.28478, respectively, representing increases of 77.4% and 88.4%. In comparison, the lateral deformation coefficient of the NAPR with 10% rubber content did not change significantly under low and high impact energies, indicating a more stable deformation state.

4.2. Deformation of Pile Body

The strain gauges had limited detection range and deformation area on the pile body. In order to obtain the local strain field evolution characteristics [33], three-dimensional digital speckle (DIC) technology was used to detect the deformation of a part of the pile body during the hammer impact test process. The deformation characteristics of NAPR with different rubber contents were similar during the hammer impact process. As shown in Figure 13, taking the local axial strain and displacement contours of the pile under 60 kJ energy impact without rubber as an example, it can be found that the deformation of the pile went through three stages according to the strain contour. The first stage was the stress wave generated by the hammer impact propagating downwards from the impact end. In the second stage, the stress wave reached the bottom pressure plate and partly propagated vertically in the opposite direction in the form of an emission wave. The pile still had some downward stress waves from the hammer impact. In the third stage, after the hammer impact, the pile mainly had the upward reflected wave left. In contrast to the strain, the distribution of displacement during impact was not uniform, as observed from the change in the displacement contour in Figure 13b. The displacement contour at the impacted end was concave-arc-shaped, with greater deformation on the outer side and smaller deformation on the inner side. The fixed end at the bottom was opposite to this,

with a convex-arc-shaped displacement contour and greater deformation on the inner side and smaller deformation on the outer side.

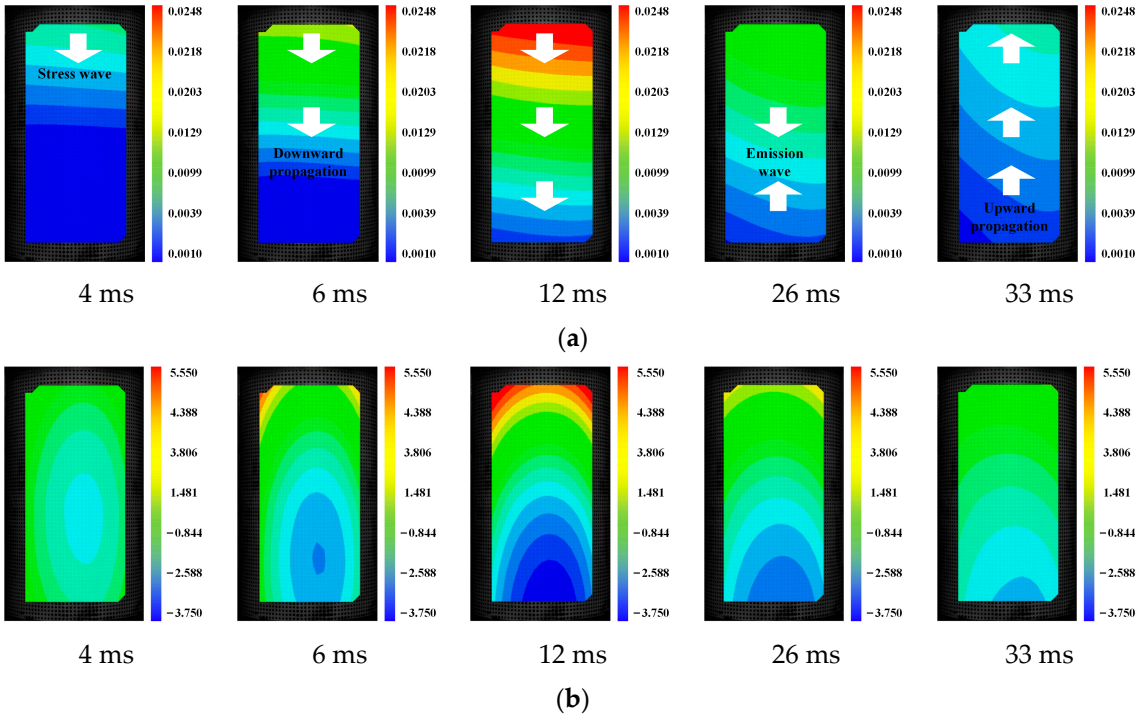


Figure 13. Deformation contours of pipe pile body under hammer impact: (**a**) Axial strains; (**b**) Axial displacements.

The deformation of NAPR bodies is mainly influenced by the impact energy. As shown in Figure 14, taking the example of NAPR without rubber, five monitoring points were arranged along the vertical direction of the pile body to detect the strains at different positions of the pile under different impact energies. The distance between adjacent monitoring points was 150 mm.

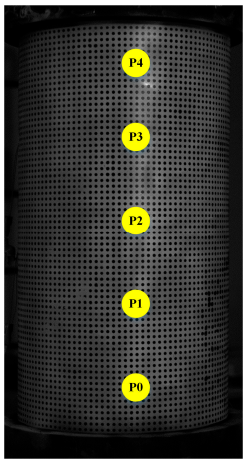
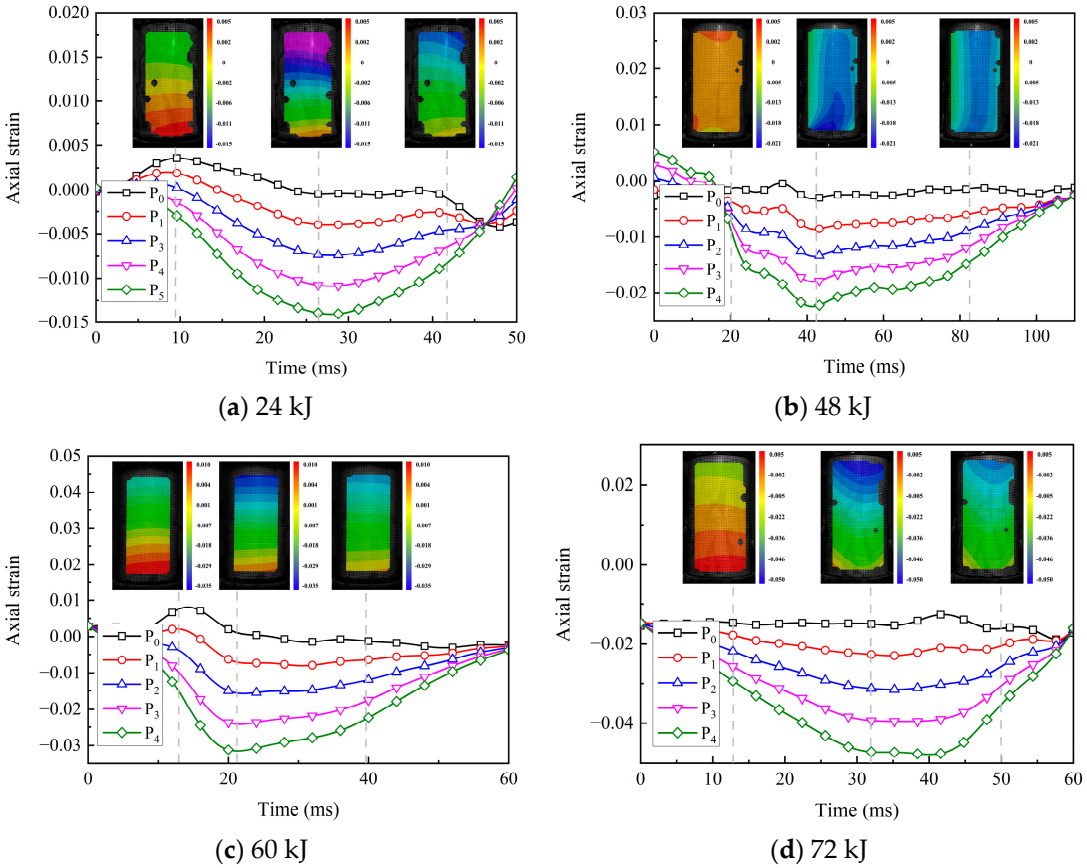


Figure 14. Layout of detection points.

As shown in Figure 15, with the increase in impact energy, the strains at various parts of the pile body increased, and the strains were greater closer to the impacted end. According to the strain values and strain contours corresponding to different time points, it could be found that before the strain reached its peak value, the deformation of the pile body was mainly in the first stage, i.e., influenced by the downward impact stress wave.

After the strain reached its peak value, it entered the second stage, where the upward reflected wave gradually affected the deformation of the pile body. Finally, when the strain decreased further, the deformation of the pile body entered the third stage, where only the upward reflected wave remained. Comparing the strain values at position P_4 under different impact energies, it was found that the strain values under four different impact energies were 0.01411, 0.02242, 0.03156, and 0.04783, respectively, and the maximum strain occurred within 30~40 ms. Comparing the strains under three different impact energies of 24 kJ, 48 kJ, and 72 kJ, it was found that their strain growth rates were 58.89% and 113.34%, respectively, indicating that the strain growth rate increased with the increasing impact energy.



(**a**) 24 kJ (**b**) 48 kJ

(**c**) 60 kJ (**d**) 72 kJ

Figure 15. Strain evolutions of pipe pile body under different impact energies.

Taking the strain at point P_4 as the research object, the deformation characteristics of NAPR with different rubber contents under different impact energies were compared. As shown in Figure 16, the strain of the NAPR at the impact end generally increased with the increasing rubber content. The reason why the strain of the pile with 5% rubber content was the largest under the impact energy of 48 kJ was that all piles with different rubber contents began to show a small amount of damage under this impact load, and the pile with 5% content had the greatest brittleness. When it was damaged, brittle fracture was the main mode, and the deformation produced was larger than in other NAPR with different rubber contents. However, with the further increase in impact energy, other NAPR with different rubber contents also showed larger deformation and the measured strain once again met the rule of increasing with the increasing rubber content. In addition, when the impact energy was less than 72 kJ, the deformation time of the pile with 15% rubber content was longer, indicating that its energy absorption effect was good. However, when the impact energy was 72 kJ, its deformation time was significantly shortened, because this impact energy

exceeded its absorption limit, and an obvious impact hardening phenomenon appeared in the pile.

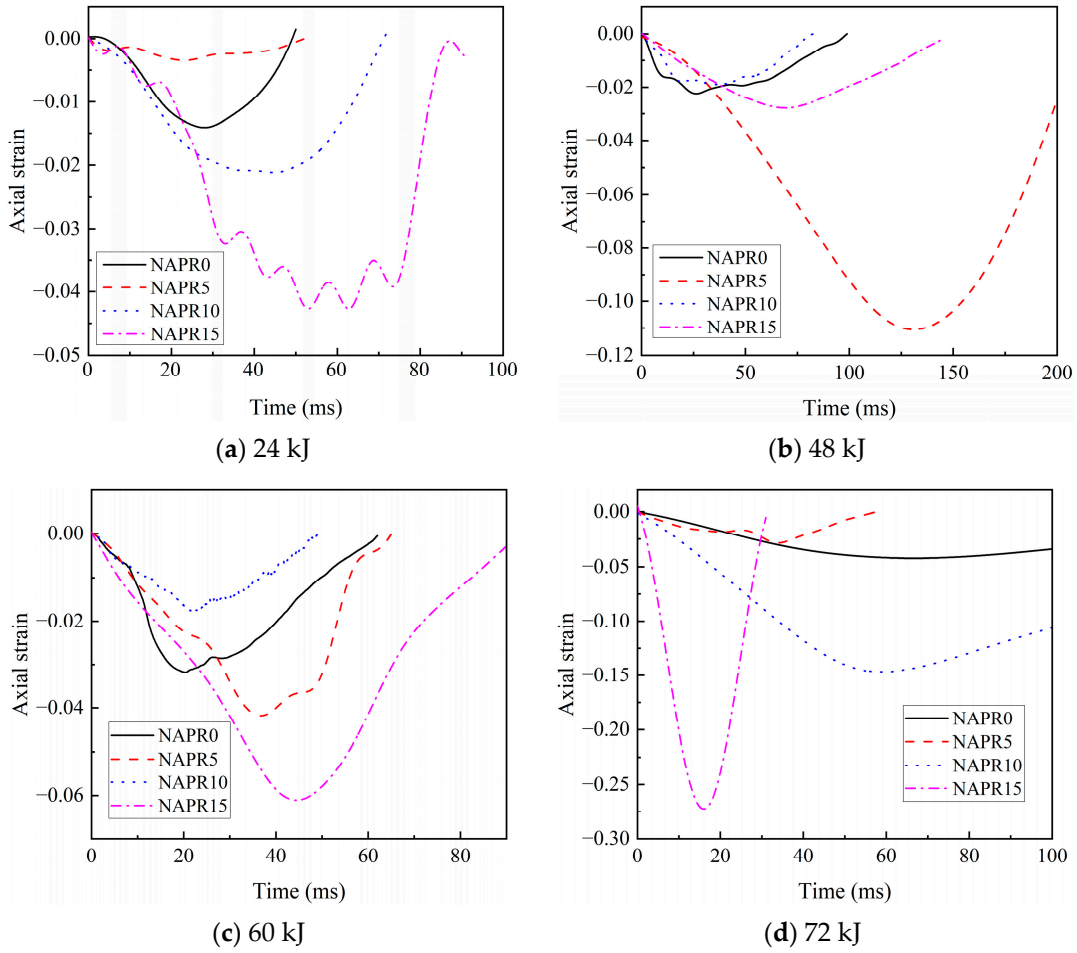


Figure 16. Strain evolutions of NAPR with different rubber contents.

4.3. Damage to Pipe Piles

4.3.1. Failure Modes

The failure mode of NAPR under axial hammer impact is also an expression of its dynamic performance. As shown in Figure 17, taking the rubber content of 15% and the impact energy of 72 kJ as an example, when subjected to a drop hammer impact, cracks began to appear at the impacted end of the pipe pile. With the further increase in the impact load, these cracks started to develop along the axial and transverse directions, eventually forming a crack network, and clear damage appeared near the end of the pipe pile.

Figure 18 illustrates the failure modes of NAPR with different rubber contents under various impact energies. When the impact energy was 24 kJ, the pile bodies of NAPR with different rubber contents remained intact, and no defects or cracks were observed on the inner and outer walls. When the impact energy was 48 kJ, the impact load caused plastic deformation of the concrete material in the NAPR, resulting in damage for piles with different rubber contents. For 0% and 5% rubber contents, large block-like fractures appeared at the bottom of the NAPR, with the most severe fracture occurring at 5% rubber content. At 10% rubber content, a long, slender crack appeared in the pile body. With 15% rubber content, only a few small microcracks appeared at the bottom of the pile. Therefore, it was evident that rubber significantly reduced pile damage under low impact energy.

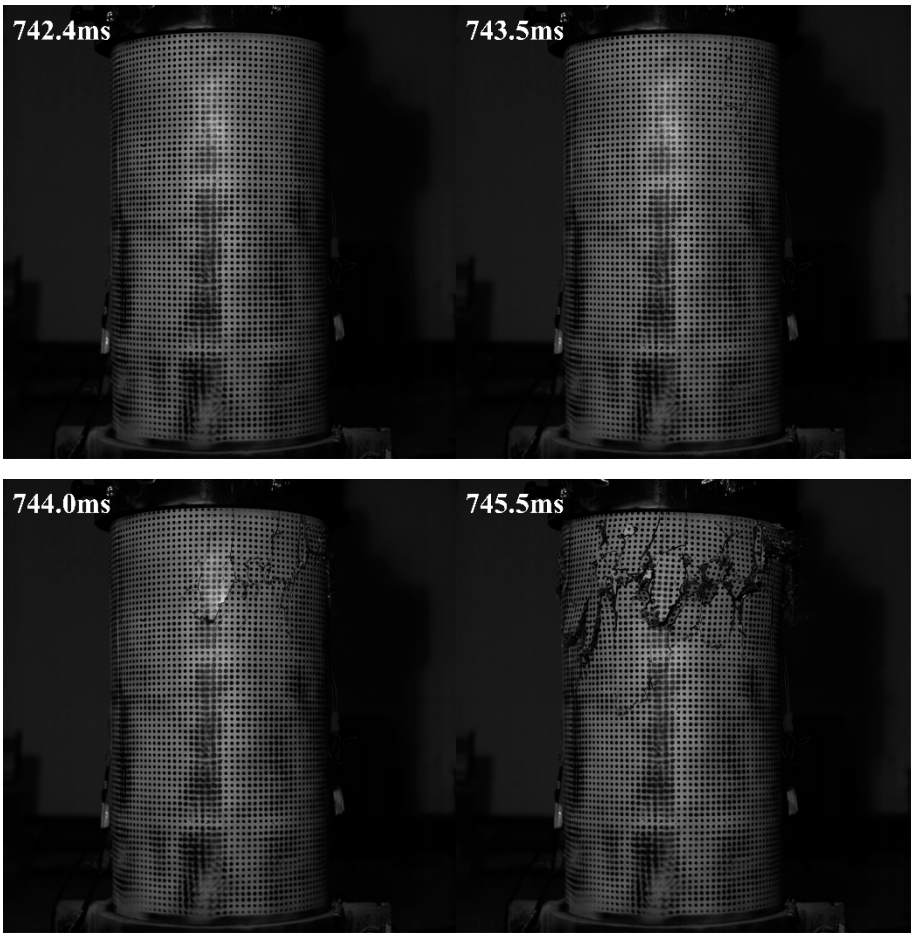
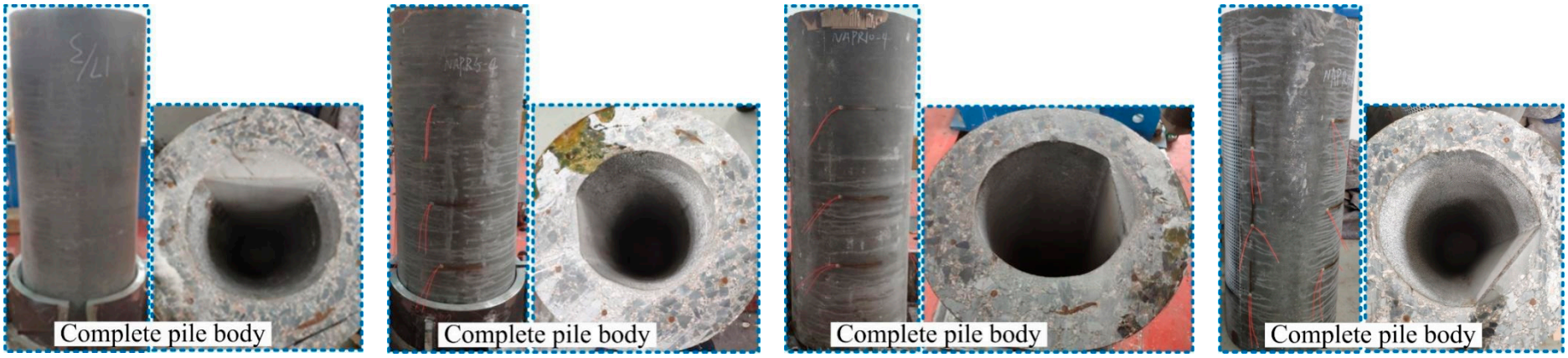


Figure 17. The process of axial hammer impact on NAPR.

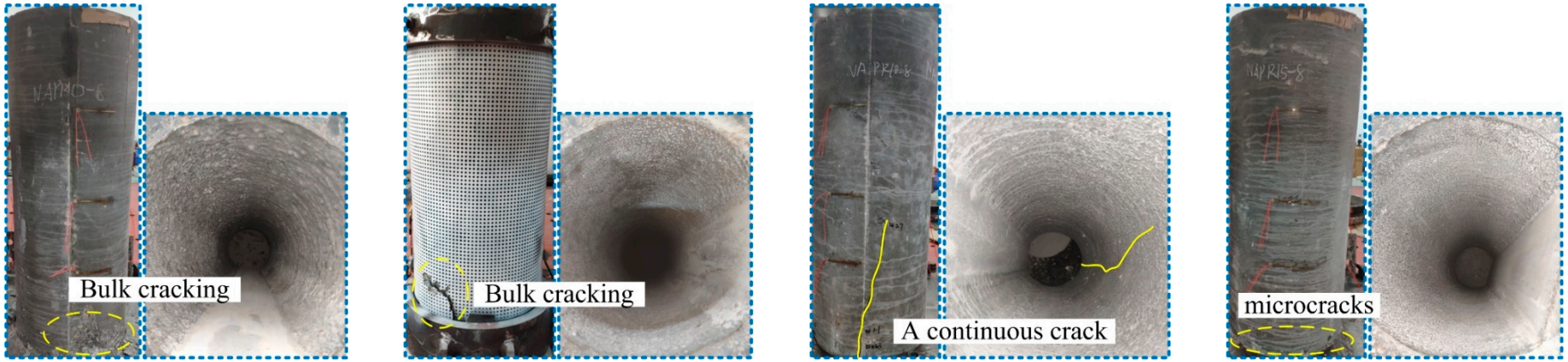
When the impact energy reached 60 kJ, it fell into the high impact energy range, and NAPR with different rubber contents all experienced plastic deformation and significant damage. With 0% rubber content, three axial cracks connecting the upper and lower ends of the pile appeared on the outer wall. With 5% rubber content, two axial cracks penetrating the pile body appeared, with the least number of cracks. With 10% rubber content, the pile body of the piles showed three axial through cracks, similar to the damage observed when no rubber was added. With 15% rubber content, a large number of axial cracks appeared in the pile body, and several transverse cracks were also generated. This was because the concrete material in the NAPR with this content had weaker strength, and under the influence of reflected stress waves, the tensile stress generated exceeded the tensile strength of the concrete material.

When the impact energy was 72 kJ, the NAPR exhibited significant deformation and extensive damage. With 0% rubber content, the pile body showed a dense network of cracks, primarily consisting of numerous axial splitting cracks and some transverse cracks, and even a small area of collapse and fracture. With 5% rubber content, the pile body exhibited axial and transverse cracks, but compared to other rubber content levels, this concentration had the smallest number of cracks. With 10% rubber content, the pile body near the impact end experienced extensive cracking and damage, with the pile tilting and deforming. With 15% rubber content, the pile body near the impact end also underwent extensive cracking, and the bond between the steel reinforcement and concrete became weak, resulting in exposed reinforcement. This was because the bond strength between the concrete and steel reinforcement was insufficient to meet the normal working performance of the pipe pile.



NAPR0 NAPR5 NAPR10 NAPR15

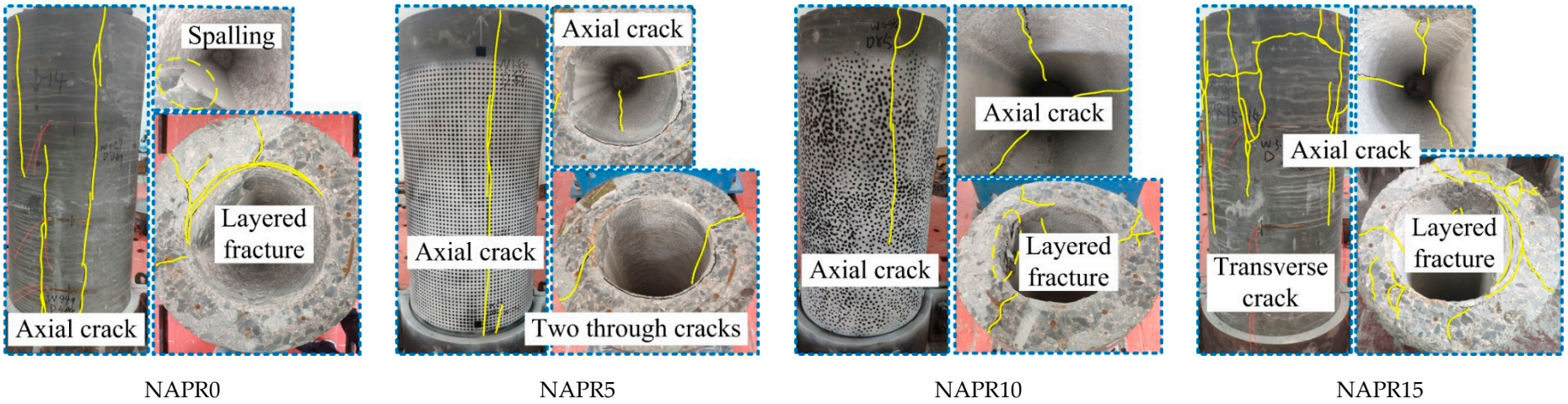
(**a**) Impact energy 24 kJ



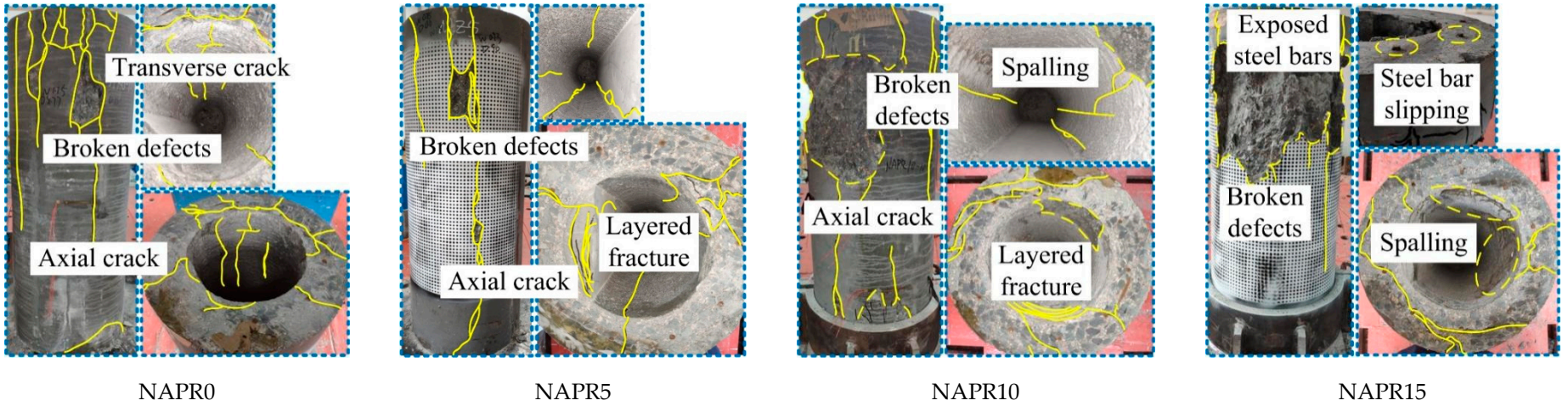
NAPR0 NAPR5 NAPR10 NAPR15

(**b**) Impact energy 48 kJ

Figure 18. *Cont*.



(**c**) Impact energy 60 kJ



(**d**) Impact energy 72 kJ

Figure 18. Failure modes of NAPR under different impact energies.

4.3.2. Damage Levels

The damage degrees of NAPR under different impact energies were divided into four levels: no damage, mild damage, moderate damage, and severe damage. Only local damage or minor cracks constituted mild damage. The appearance of several through cracks constituted moderate damage. The appearance of a crack network, and even the occurrence of severe localized damage resulting in loss of working performance, constituted severe damage. Combining the damage degree, an analysis of the momentum and load results of NAPR yielded the corresponding damage level division area. In explosions and impact loads, the steel reinforcement ratio and concrete material were the key factors determining the damage of concrete components [34], and except for the differences in the rubber and sand contents, the four types of NAPR, including morphology, reinforcement ratio, cement matrix, etc., were all the same. Therefore, the division function of different damage levels could be approximately considered the same. Taking the division function of the severe damage area of the NAPR with 15% rubber content as the benchmark function for damage level, the divisions of the damage level areas of NAPR with different rubber contents were performed, and the benchmark function is shown in Figure 19d.

As shown in Figure 19, when the NAPR was subjected to impact from a drop hammer, the damage level corresponded to the allocated damage grade region. Without adding rubber, the NAPR would experience at least mild damage when the impact exceeded 8.9 kN·s and the load exceeded 2606.7 kN. When the impact exceeded 16.1 kN·s and the load exceeded 4390.8 kN, the pile would experience at least moderate damage. Severe damage would occur when the impact exceeded 22.0 kN·s and the load exceeded 5998.6 kN. With a rubber content of 5%, the NAPR would experience at least mild damage when the impact exceeded 10.1 kN·s and the load exceeded 2184.9 kN. Moderate damage would occur when the impact exceeded 20.5 kN·s and the load exceeded 5309.6 kN. Severe damage would occur when the impact exceeded 25.6 kN·s and the load exceeded 6256.9 kN. With a rubber content of 10%, the NAPR would experience at least mild damage when the impact exceeded 12.1 kN·s and the load exceeded 3611.7 kN. Moderate damage would occur when the impact exceeded 18.7 kN·s and the load exceeded 5561.2 kN. Severe damage would occur when the impact exceeded 24.8 kN·s and the load exceeded 7010.0 kN. With the rubber content of 15%, the NAPR would experience at least mild damage when the impact exceeded 8.3 kN·s and the load exceeded 3007.0 kN. Moderate damage would occur when the impact exceeded 14.7 kN·s and the load exceeded 4400.0 kN. Severe damage would occur when the impact exceeded 20.0 kN·s and the load exceeded 5606.7 kN. It could be observed that when the rubber content was 15%, the NAPR required the minimum impact and load to form mild, moderate, and severe damage. When the rubber content was 10%, the NAPR required the highest impulse and impact load to form mild damage, indicating its strong resistance to damage.

To further analyze the influence of rubber on the impact damage of NAPR, the areas of each damage grade region of various rubber contents at impulse of 308.3 kN.s and load of 8000.0 kN were compared. As shown in Figure 20, it could be observed that the zone of no damage was the largest for the NAPR with a rubber content of 10%. This indicated that the 10% rubber content provided better resistance to damage and optimal impact resistance performance. The zone of mild damage was the largest for the NAPR with a rubber content of 5%, indicating that this content was more prone to mild damage. The zones of mild, moderate, and severe damage were all larger for the NAPR with a rubber content of 15%, especially for severe damage, which had the highest proportion. This indicated that the NAPR with a 15% rubber content were more susceptible to severe damage. This was because the excessive rubber content significantly reduced the strength of the NAPR concrete itself and the bond strength with the steel reinforcement.

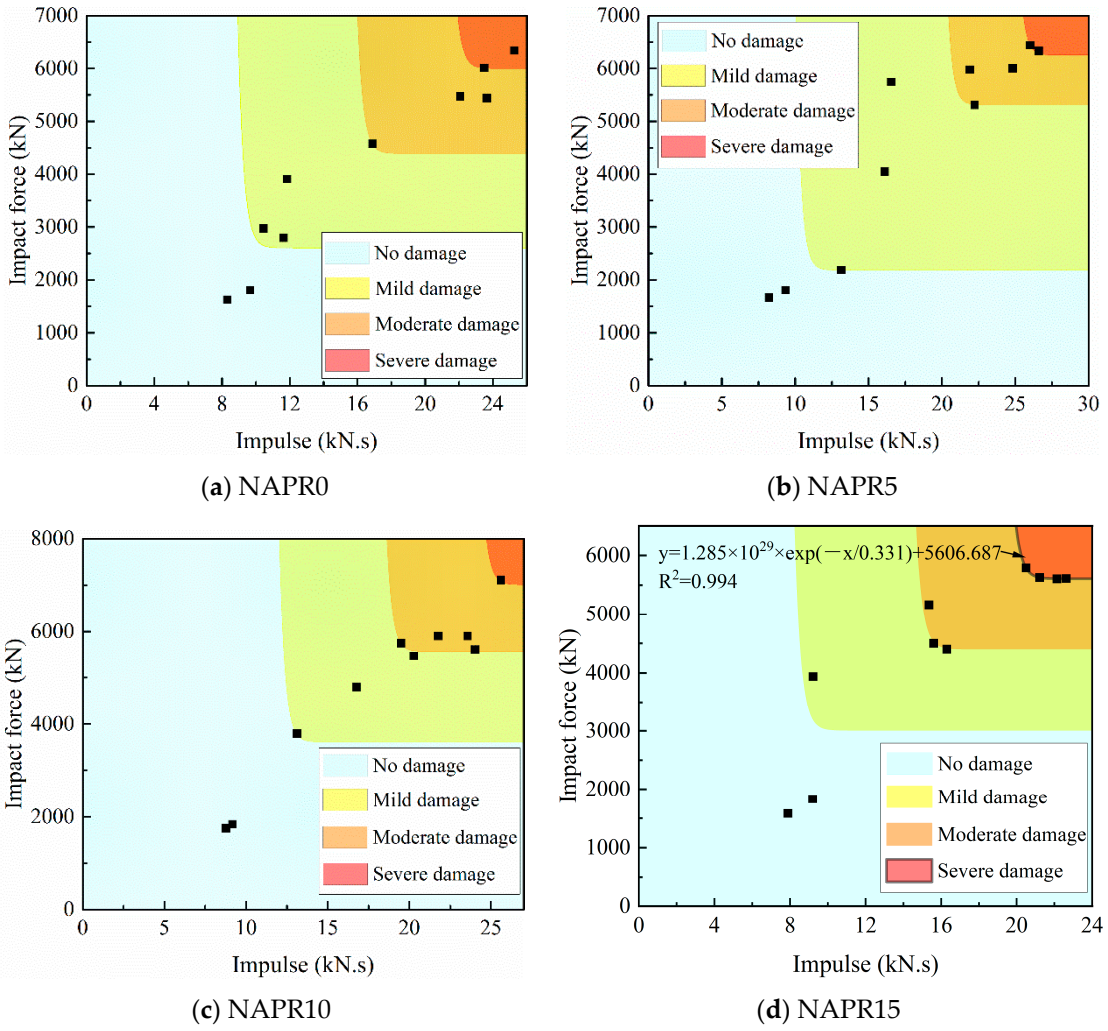


Figure 19. Classification of impact damage levels for NAPR.

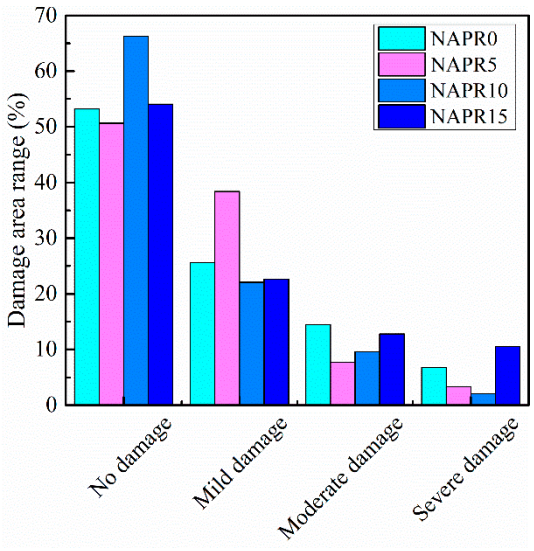


Figure 20. Damage evaluation of NAPR with different rubber contents.

5. Conclusions

Based on the results obtained from the axial drop hammer impact tests conducted on NAPR, the following conclusions can be drawn.

(1) When subjected to low impact energy (less than 48 kJ) impacts, the impact load of NAPR was minimally affected by the rubber content. When subjected to high impact energy (greater than 48 kJ) impacts, the impact load of NAPR increased initially and then decreased with the increasing rubber content, with the maximum impact load occurring at a 5% content level.

(2) When the impact energy was less than 48 kJ, the deformation energies produced by NAPR with various rubber contents during the drop hammer impact process were similar. However, as the impact energy increased, the deformation energies of NAPR with 5% and 10% rubber contents increased significantly.

(3) When no rubber particles were added, the NAPR exhibited a pronounced trend of expansion deformation under axial impact. With the increase in rubber content, the axial deformation of NAPR increased. However, at higher impact energies (72 kJ), the 5% and 15% rubber content piles also showed trends of expansion deformation, whereas only the NAPR with 10% rubber content exhibited a smaller lateral deformation coefficient, making them less susceptible to instability failure.

(4) When the impact energy exceeded 48 kJ, NAPR exhibited damage, which is categorized into four levels: no damage, mild damage, moderate damage, and severe damage. Among these, the piles with 10% rubber content had the largest undamaged area, while those with 5% rubber content were most susceptible to damage, and those with 15% rubber content were even more prone to severe damage.

(5) Based on the deformation, deformation energy, and damage degree of NAPR in the axial drop hammer tests, it can be found that the pipe pile had the best deformation and energy absorption effects when the rubber content was 10%, and it was also the most difficult to damage. It exhibited excellent impact resistance. The best rubber content, ultimate bearing capacity, and damage level evaluation obtained in the tests can provide an important basis for subsequent on-site NAPR impact tests and durability tests.

Author Contributions: Writing—original draft, S.L.; Writing—review & editing, F.L., F.Y., W.F. and D.C. All authors have read and agreed to the published version of the manuscript.

Funding: This research was funded by [the National Natural Science Foundation of China] grant number [12072080], [the National Natural Science Foundation of China] grant number [12072079], [the Science and Technology Planning Project of Guangzhou City] grant number [202002030120], [Special Foundation for Scientific and Technological Innovation Strategy of Guangdong Province] grant number [pdjh2022a0147], [Guangdong Basic and Applied Basic Research Foundation] grant number [2022A1515010008], [Guangdong Basic and Applied Basic Research Foundation] grant number [2023A1515010870].

Data Availability Statement: The data presented in this study are available in the article.

Acknowledgments: The authors gratefully acknowledge the financial support provided by the National Natural Science Foundation of China under Grant Nos. 12072080 and 12072079, the Science and Technology Planning Project of Guangzhou City under Grant No. 202002030120 (in China), Special Foundation for Scientific and Technological Innovation Strategy of Guangdong Province under Grant No. pdjh2022a0147 (in China), and Guangdong Basic and Applied Basic Research Foundation under Grant Nos. 2022A1515010008 (in China) and 2023A1515010870 (in China).

Conflicts of Interest: The authors declare no conflict of interest.

References

1. Qi, Z.; Liu, F.; Deng, M.; Hu, J. Research on cleaner production potential of pipe pile industry based on material energy flow analysis. In *IOP Conference Series: Earth and Environmental Science*; IOP Publishing: Bristol, UK, 2021; Volume 621, p. 012161.
2. Wu, Z.; Huang, H.; Chen, X.; Li, J.; He, Q.; Li, A.; Huang, J.; Lin, Y.; Liu, X.; Wang, J. Countermeasures for low-carbon transformation of construction industry in China toward the carbon peaking and carbon neutrality goals. *Strateg. Study CAE* **2023**, *25*, 202–209. [CrossRef]

3. Sonibare, J.A.; Akeredolu, F.A. A theoretical prediction of non-methane gaseous emissions from natural gas combustion. *Energy Policy* **2004**, *32*, 1653–1665. [CrossRef]
4. *T/CBMF 27-2018*; Methods and Requirements of Low-Carbon Products Evaluation for Ready-Mixed Concrete. China Building Materials Federation: Beijing, China, 2018.
5. Li, G.; Chen, X.; Zhang, Y.; Zhuang, Z.; Lv, Y. Studies of nano-SiO_2 and subsequent water curing on enhancing the frost resistance of autoclaved PHC pipe pile concrete. *J. Build. Eng.* **2023**, *69*, 106209. [CrossRef]
6. Hu, Y.; Ma, L.; He, T. Effect of mineral admixtures on the sulfate resistance of high-strength piles mortar. *Materials* **2020**, *13*, 3500. [CrossRef] [PubMed]
7. Tan, K.; Zhu, J. Influences of steam and autoclave curing on the strength and chloride permeability of high strength concrete. *Mater. Struct.* **2017**, *50*, 56. [CrossRef]
8. Zhan, Y.; Yang, Y.; Wu, X.; Xie, Y.; Luo, J.; Guo, W.; Hao, Y.; Wang, H. Experimental study on non-autoclaved PHC pile concrete applying polycarboxylate superplasticizer. *Key Eng. Mater.* **2015**, *629–630*, 345–350. [CrossRef]
9. Lan, S.; Liu, F.; Yang, F.; Li, H.; Chen, D.; Xu, K.; Zhang, H.; Kuang, J.; Fang, Z.; Feng, W. Dynamic compressive and splitting tensile characteristics of rubber-modified non-autoclaved concrete pipe piles. *J. Build. Eng.* **2023**, *69*, 106292. [CrossRef]
10. Liu, F.; Feng, W.; Xiong, Z.; Li, L.; Yang, Y.; Lin, H.; Shen, Y. Impact performance of new prestressed high-performance concrete pipe piles manufactured with an environmentally friendly technique. *J. Clean. Prod.* **2019**, *231*, 683–697. [CrossRef]
11. Thanaraj, D.P.; Anand, N.; Arulraj, P. Experimental investigation of mechanical properties and physical characteristics of concrete under standard fire exposure. *J. Eng. Des. Technol.* **2019**, *17*, 878–903. [CrossRef]
12. Zhu, H.; Xiong, Z.; Song, Y.; Zhou, K.; Su, Y. Effect of expansion agent and glass fiber on the dynamic splitting tensile properties of seawater–sea-sand concrete. *Buildings* **2024**, *14*, 217. [CrossRef]
13. Zhen, H.; Xiong, Z.; Song, Y.; Li, L.; Qiu, Y.; Zou, X.; Chen, B.; Chen, D.; Liu, F.; Ji, Y. Early mechanical performance of glass fibre-reinforced manufactured sand concrete. *J. Build. Eng.* **2024**, *83*, 108440. [CrossRef]
14. Fang, Z.; Wu, J.; Zhao, G.; Fang, S.; Ma, Y.; Jiang, H. Shear performance and design recommendations of single embedded nut bolted shear connectors in prefabricated steel–UHPC composite beams. *Steel Compos. Struct.* **2024**, *50*, 319–336.
15. Ding, Y.; Zhang, J.; Chen, X.; Wang, X.; Jia, Y.; Yan, P. Experimental study on dynamic parameter characteristics of new subgrade filler composed of granular rubber-sand mixtures. *Adv. Eng. Sci.* **2020**, *52*, 170–177.
16. Thomas, B.S.; Gupta, R.C. Properties of high strength concrete containing scrap tire rubber. *J. Clean. Prod.* **2016**, *113*, 86–92. [CrossRef]
17. Mendis, A.S.M.; Al-Deen, S.; Ashraf, M. Effect of rubber particles on the flexural behaviour of reinforced crumbed rubber concrete beams. *Constr. Build. Mater.* **2017**, *154*, 644–657. [CrossRef]
18. Bompa, D.V.; Elghazouli, A.Y. Creep properties of recycled tyre rubber concrete. *Constr. Build. Mater.* **2019**, *209*, 126–134. [CrossRef]
19. Chan, C.; Yu, T.; Zhang, S.; Xu, Q. Compressive behaviour of FRP-confined rubber concrete. *Constr. Build. Mater.* **2019**, *211*, 416–426. [CrossRef]
20. Eltayeb, E.; Ma, X.; Zhuge, Y.; Youssf, O.; Mills, J.E. Influence of rubber particles on the properties of foam concrete. *J. Build. Eng.* **2020**, *30*, 101217. [CrossRef]
21. Pan, Z.; Liu, F.; Li, H.; Li, X.; Wang, D.; Ling, Z.; Zhu, H.; Zhu, Y. Performance evaluation of thermal insulation rubberized mortar modified by fly ash and glass fiber. *Buildings* **2024**, *14*, 221. [CrossRef]
22. Klimesch, D.S.; Ray, A.; Sloane, B. Autoclaved cement-quartz pastes: The effects on chemical and physical properties when using ground quartz with different surface areas Part I: Quartz of wide particle size distribution. *Cem. Concr. Res.* **1996**, *26*, 1399–1408. [CrossRef]
23. *GB/T 13476-2009*; Pretensioned Spun Concrete Piles. General Administration of Quality Supervision, Inspection and Quarantine of the People's Republic of China and Standardization Administration of the People's Republic of China: Beijing, China, 2009.
24. *JGJ/T 406-2017*; Technical Standard for Prestressed Concrete Pipe Pile. Ministry of Housing and Urban-Rural Development of the People's Republic of China: Beijing, China, 2017.
25. Michele, G.; Mathias, F.; Williams, N.P. Low-velocity out-of-plane impact tests on double-wythe unreinforced brick masonry walls instrumented with optical measurements. *Int. J. Impact Eng.* **2023**, *178*, 104597.
26. *JGJ 94*; Technical Code for Building Pile Foundations. Ministry of Construction of the People's Republic of China: Beijing, China, 1994.
27. Fellenius, H.B.; Altaee, A.; Ismael, F.N. Analysis of load tests on piles driven through calcareous desert sands. *J. Geotech. Geoenviron. Eng.* **2001**, *127*, 200–201. [CrossRef]
28. Altaee, A.; Fellenius, B.H.; Evgin, E. Axial load transfer for piles in sand. I. Tests on an instrumented precast pile. *Can. Geotech. J.* **1992**, *29*, 11–20. [CrossRef]
29. Fellenius, B.H.; Samson, L. Testing of drivability of concrete piles and disturbance to sensitive clay. *Can. Geotech. J.* **1976**, *13*, 139–160. [CrossRef]
30. Martin, R.E.; Seli, J.J.; Powell, G.W.; Bertoulin, M. Concrete pile design in tidewater Virginia. *J. Geotech. Eng.* **1987**, *113*, 568–585. [CrossRef]
31. Zhao, C.; Lei, M.; Jia, C.; Yang, Z.; Shi, Y. An elastoplastic damage model for concrete considering the influence of mesostructure on transverse deformation. *Constr. Build. Mater.* **2023**, *406*, 133458. [CrossRef]

32. Xiao, C.; Gao, S.; Han, J.; Ding, L. Lateral facing deformation versus factor of safety for geosynthetic-reinforced soil walls in a tiered configuration. *Transp. Geotech.* **2023**, *41*, 101018. [CrossRef]
33. De Wilder, K.; Lava, P.; Debruyne, D.; Wang, Y.; de Roeck, G.; Vandewalle, L. Experimental investigation on the shear capacity of prestressed concrete beams using digital image correlation. *Eng. Struct.* **2015**, *82*, 82–92. [CrossRef]
34. Yan, Q.S. Damage assessment of subway station columns subjected to blast loadings. *Int. J. Struct. Stab. Dyn.* **2018**, *18*, 1850034. [CrossRef]

Disclaimer/Publisher's Note: The statements, opinions and data contained in all publications are solely those of the individual author(s) and contributor(s) and not of MDPI and/or the editor(s). MDPI and/or the editor(s) disclaim responsibility for any injury to people or property resulting from any ideas, methods, instructions or products referred to in the content.